Computation of Aeroacoustic Sound Via Hybrid CFD/CAA-Methods

R. Ewert[1], M. Meinke[2], W. Schröder[3]
Aerodynamisches Institut
RWTH Aachen, Wüllnerstraße zw. 5 und 7
52062 Aachen, Germany

[1] Research Scientist, e-mail: roland@aia.rwth-aachen.de
[2] Senior Scientist, e-mail: matthias@aia.rwth-aachen.de
[3] Professor, Dept. Mechanical Engineering, e-mail: office@aia.rwth-aachen.de

Different formulations for a two step CFD/CAA approach are investigated. The acoustic field is simulated using linearized perturbation equations which are excited by sources determined from the unsteady compressible near field flow. The sound generated by a cylinder in laminar flow at Mach number M=0.3 and Reynolds number Re=200 is used as a test problem. It is examined whether the viscous/acoustic splitting method of Shen et al., which is based on a simulation of the incompressible flow field, can be adapted to a compressible base flow simulation. It is found that excessive artificial vorticity is generated in the wake of the cylinder due to the excitation of hydrodynamic instabilities. A new set of governing acoustic perturbation equations (APE) is proposed, which includes sources determined from a compressible flow simulation. As shown for the test problem, the occurrence of vorticity is prevented completely since the source solely excites acoustic modes in the APE.

1 Introduction

The future goal of this research is the development of computational tools to simulate turbulence related noise. The hybrid approach investigated in this paper predicts the acoustic field using a two step procedure. To motivate this approach we briefly consider the noise generated by the turbulent flow in the vicinity of a flat plate, fig. 1. In the first step, the unsteady compressible flow field in the vicinity of the sharp trailing edge is simulated via a large eddy simulation (LES) [3,8]. Fig. 1 shows a sketch of the computational domain used for the LES. Due to the large disparity in acoustic and hydrodynamic length scales, whose ratio scales inversely proportional to the Mach number, as well as energy levels [9], the demands concerning grid resolution, grid size, boundary conditions, and time steps differ for fluid and acoustic simulations. The larger acoustic length scale allows to use coarser grids for a pure acoustic simulation. Therefore, the acoustic field is computed with linearized perturbation equations in a second step using sources determined from the unsteady compressible flow field. The integration domain of the acoustic computation contains the whole plate. Hence, it allows to recognize diffraction at the leading edge and the prediction of directivities. This paper focuses on a comparison of different perturbation equations and source formulations. The laminar flow over a cylinder at a Mach $M=0.3$ and a Reynolds number $Re=200$ is considered as a test problem for this analysis. First, a direct numerical simulation is conducted that provides a reference solution. Subsequently, several source term formulations are applied to the cylinder flow. The results of the computation of the acoustic field are juxtaposed to evidence the characteristics of the various approaches.

Paper presented at the RTO AVT Symposium on "Ageing Mechanisms and Control: Part A – Developments in Computational Aero- and Hydro-Acoustics", held in Manchester, UK, 8-11 October 2001, and published in RTO-MP-079(I).

2 Numerical Method

2.1 Discretization of the linearized perturbation equations

The aeroacoustic computations are based on linearized perturbation equations, which can be written including a source term $\boldsymbol{S}$ for a non-uniform flow in Cartesian coordinates (x_1, x_2)

$$\frac{\partial \mathbf{U}}{\partial t} + \mathbf{A}_i \frac{\partial \mathbf{U}}{\partial x_i} + \mathbf{B} \cdot \mathbf{U} = \mathbf{S}, \tag{1}$$

where $\boldsymbol{U}$ is the vector of the primitive variables of the perturbation quantities. Einstein's summation convention is to be applied to the products with equal indices. To use body fitted grids the governing equations are transformed to generalized curvilinear coordinates (ξ_1, ξ_2)

$$\frac{\partial \mathbf{U}}{\partial t} + \hat{\mathbf{A}}_i \frac{\partial \mathbf{U}}{\partial \xi_i} + \mathbf{B} \cdot \mathbf{U} = \mathbf{S} \qquad \text{with} \qquad \hat{\mathbf{A}}_i = \mathbf{A}_j \frac{\partial \xi_i}{\partial x_j}. \tag{2}$$

For the spatial discretization of eq. (2) the fourth-order dispersion relation preserving (DRP) scheme of Tam and Webb [10] is used. This scheme is designed such that for a wide range of wavenumbers the dispersion relations of the numerical scheme matches the physical dispersion relations. A first derivative with respect to a curvilinear direction ξ_1 is calculated for a quantity $f_{l,m}$ at mesh point l,m with a seven point stencil via

$$\left(\frac{\partial f}{\partial \xi_i}\right)_{l,m} = \sum_{j=-3}^{3} a_j f_{l+j,m.}$$

Appropriate coefficients a_j of the DRP-scheme minimize the difference between the physical and numerical dispersion relation over a chosen range of wavelengths and frequencies. In order to achieve fourth-order accuracy six of the coefficient are determined by constraints following from a Taylor series expansion around point l,m , while the one remaining can be used to minimize the dispersive error. The DRP-scheme yields a resolution of about 5.4 points per wavelength (PPW), while a central difference scheme of second order yields the same resolution limit with 20 PPW, therefore for 3D-applications the number of points can be reduced approximatly two orders of magnitude, compared to mainstream CFD spatial discretization methods.

Close to boundaries one-sided stencils are used. The integration in time is carried out with the fourth-order alternating two-step low dissipation and low dispersion Runge-Kutta scheme (LDDRK 5-6) proposed by Hu [11]. To suppress spurious high frequency waves artificial selective damping (ASD) according to Tam and Dong [13] has been used. The ASD is given as an additional source term $\boldsymbol{S}_{l,m}$ in eq. (1) by

$$\mathbf{S}_{l,m} = -\frac{1}{\Delta_{\xi_1} \mathrm{Re}_\Delta} \sum_{j=-3}^{3} d_j \mathbf{U}^n_{l+j,m} - \frac{1}{\Delta_{\xi_2} \mathrm{Re}_\Delta} \sum_{j=-3}^{3} d_i \mathbf{U}^n_{l,m+i}, \quad \Delta_{\xi_i} = \sqrt{\left(\frac{\partial x_1}{\partial \xi_i}\right)^2 + \left(\frac{\partial x_2}{\partial \xi_i}\right)^2},$$

where Re_Δ is the mesh Reynolds numer. The coordinates x_i are nondimensionalized with a reference length. The scaling of the damping with the grid size is chosen such that the magnitude of the mesh Reynolds number is nearly constant for a homogeneous damping effect on a mesh with variable cell size. A constant background value of the mesh Reynolds number with a typical value of $1/\mathrm{Re}_\Delta = 0.05$ and a slight increase close to boundaries is used. The damping term provides a wavenumber dependent damping such that long waves with scaled wavenumbers ≤ 1 are nearly unaffected.

3 Governing acoustic equations

3.1 Viscous/Acoustic Splitting Methods

The first formulation examined in this paper is based on the viscous/acoustic splitting technique first proposed by Hardin and Pope [14,15] later modified by Shen and Sorensen [16,17].Using Cartesian tensor notations the governing acoustic equations read

$$\begin{aligned}
&\frac{\partial \rho'}{\partial t}+\frac{\partial f_i}{\partial x_i}=0,\\
&\frac{\partial f_i}{\partial t}+\frac{\partial}{\partial x_j}\left[f_i\left(U_j+u'_j\right)+\rho_\infty U_i u'_j+p'\delta_{ij}\right]=0,\\
&\frac{\partial p'}{\partial t}-c^2\frac{\partial \rho'}{\partial t}=-\frac{\partial P}{\partial t}
\end{aligned} \tag{3}$$

with $f_i = \rho u'_i + \rho' U_i$. In these equations the flow variables are decomposed into incompressible and compressible primed perturbation variables

$$u_i = U_i + u'_i, \quad p = P + p', \quad \rho = \rho_\infty + \rho'.$$

The equations (3) are derived by introducing the decomposition of the flow variables into the Navier-Stokes and the continuity equation and by subtracting the governing equations for incompressible flow. Furthermore, the difference between compressible and incompressible viscous terms is neglected. As explained in section 3.3 the perturbation variables describe besides acoustic quantities also vorticity fluctuations due to mean/acoustic interaction. Furthermore, the difference between compressible and incompressible viscous terms is neglected. The perturbation quantities describe acoustic as well as non-acoustic unsteady and steady quantities, which determine the difference between the compressible and incompressible solutions. The third equation in (3) follows from the second law of thermodynamics. The local time derivative is used in combination with the constraint that the initial values of p', ρ' and entropy S satisfy the second law of thermodynamics. It is assumed that the time variation of the entropy can be dropped if vortex sound is considered. The unsteady incompressible velocity U_i and pressure P follow from an incompressible flow simulation. The time derivative of the incompressible pressure in eqn. (3) is the major source term for the acoustic equations. Even when the entropy is dropped in the pressure equation the relation between pressure and density is not isentropic due to the non-vanishing right-hand side. Therefore, Hardin and Pope used a further decomposition of the density into $\rho' = \rho'' + \rho_1$, where the double primed density denotes the isentropic density fluctuation related to the single primed pressure and ρ_1 is a compressible density correction caused by the incompressible pressure fluctuations. By introducing the additional density decomposition into (3), the formulation presented by Hardin et al. [15] is obtained, where additional source terms containing ρ_1 occur on the right-hand side of the continuity and momentum equation, and the continuity equation becomes a governing equation for the isentropic density perturbation. Since this component can be directly computed from the pressure via $p' = c^2\rho''$ it is computationally simpler to drop the additional density decomposition.

To associate the formulation of Shen et al. with the problem of sources determined from a compressible flow simulation, first the system (3) is linearized over the time averaged incompressible flow simulation and then using the governing incompressible equations is rewritten in primitive variables

$$\begin{aligned}
&\frac{\partial \rho'}{\partial t}+\frac{\partial}{\partial x_k}\left(\rho'\overline{U}_k+\rho_\infty u'_k\right)=0\\
&\frac{\partial u'_i}{\partial t}+\overline{U}_k\frac{\partial u'_i}{\partial x_k}+\left(u'_k+\frac{\rho'}{\rho_\infty}\overline{U}_k\right)\frac{\partial \overline{U}_i}{\partial x_k}+\frac{1}{\rho_\infty}\frac{\partial p'}{\partial x_i}=0\\
&\frac{\partial p'}{\partial t}-\overline{c}^2\frac{\partial \rho'}{\partial t}=-\frac{\partial P}{\partial t}.
\end{aligned} \tag{4}$$

For the computations the time averaged mean flow of the compressible flow simulation is used instead of the incompressible mean flow quantities since their difference is $O(M^2)$ small for low Mach numbers. If the source term of the pressure equation in (4) is computed directly from the pressure of the compressible flow

simulation, the acoustic equations are excited by the acoustic pressure fluctuations contained in the compressible solution. Due to the fact that their magnitude does not decay sufficiently fast with increasing distance to the cylinder they have a strong influence on the pressure levels computed via (4). It will be checked whether a spatial Gaussian filtering of the source in eqn. (10) is sufficient to separate the important near field hydrodynamic pressure fluctuations from the artificial far field ones. This issue will be addressed in the section results and discussion.

3.2 LEE with momentum sources

The second formulation is based on the source term formulation proposed by Bailly et al. [1]. The governing equations are the linearized Euler equations (LEE) which are linearized over the time averaged compressible flow solution. The equation written in primitive variables read

$$\begin{aligned}
&\frac{\partial \rho'}{\partial t}+\frac{\partial}{\partial x_k}\left(\rho'\bar{u}_k+\bar{\rho}u_k'\right)=0\\
&\frac{\partial u_i'}{\partial t}+\bar{u}_k\frac{\partial u_i'}{\partial x_k}+\frac{1}{\bar{\rho}}\frac{\partial p}{\partial x_i}+H_i=S_i \qquad (5)\\
&\frac{\partial p'}{\partial t}+\frac{\partial}{\partial x_k}\left(p'\bar{u}_k+\gamma\bar{p}u_k'\right)+H_p=0.
\end{aligned}$$

The terms H_i and H_p depend linearly on the perturbation quantities, where the proportionality factors are prescribed from mean flow quantities and gradients, respectively. Thus, depending on the sign of the coefficients these terms can cause an unstable growth. These expressions are neglected by Bailly et al. [1] in order to suppress the occurrence of shear layer instabilities. Variables with a bar denote time averaged quantities. The source term of the momentum equations was determined by the major non-linear contribution, i.e.,

$$S_i=-u_k'\frac{\partial u_i'}{\partial x_k}+\overline{u_k'\frac{\partial u_i'}{\partial x_k}}\,. \qquad (6)$$

The source term excites acoustic as well as vorticity components in the LEE such that the grid resolution has to be fine enough to properly resolve the vorticity components. Thus, the advantage of reduced grid resolution allowed for the simulation of pure acoustic modes is lost. The source (6) has been used with a no-slip wall boundary condition to prevent the occurence of unphysical high velocities in the vicinity of the wall.

3.3 Acoustic perturbation equations (APE)

The third formulation is based on the following acoustic perturbation equations (APE) [2]

$$\begin{aligned}
&\frac{\partial \rho'}{\partial t}+\frac{\partial f_i}{\partial x_i}=0,\\
&\frac{\partial f_i}{\partial t}+\frac{\partial}{\partial x_j}\left[f_i\left(U_j+u_j^a\right)+\rho_\infty U_i u_j^a+p^a\delta_{ij}\right]=\rho_\infty D_I\left(\omega,u_j^a\right)+\rho_\infty D_{II}\left(\rho',p,\underline{\tau}\right)+\rho' D_{III}\left(U_j,\underline{\tau}\right) \qquad (7)\\
&\frac{\partial p^a}{\partial t}-c^2\frac{\partial \rho'}{\partial t}=-\frac{\partial}{\partial t}\left(\rho_\infty\Phi\right)+\frac{\gamma p}{c_p}\frac{\partial S}{\partial t}
\end{aligned}$$

where $f_i=\rho u_i^a+\rho' U_i$. It is derived from the continuity and the Navier-Stokes equations without introducing any simplifications and follows from a decomposition of a general source vector of the linearized Euler equations into acoustic and non-acoustic contributions in Fourier-/Laplace transform space. This source term filtering [4] is valid under the constraint of using a uniform mean flow field in the LEE. An extension to non-uniform flow is possible similarly to the derivation of higher acoustic analogies from Lighthill's acoustic analogy. The extension of Lighthill's acoustic analogy to a precursor of Lilley's equation

by transferring convection terms from the source to the wave operator side was discussed by Ribner [7]. In a second step the velocities have to be substituted using the momentum equation in order to get a scalar wave equation. As shown in [2] convection effects can be taken into account in the perturbation equations by shifting convection terms to the left-hand side, too. Due to the fact that rather a system of equations is solved for all acoustic quantities than a scalar wave equation for one variable, the second step of substitution is not necessary. The system (7) is the result of that analysis. As a formal finding of the source term filtering the velocities are decomposed into irrotational acoustic variables u_i^a and unsteady solenoidal base flow velocities U_i, i.e.,

$$u_i = U_i + u_i^a .$$

The solenoidal velocity is computed from the vorticity $\omega = \partial u_2/\partial x_1 - \partial u_1/\partial x_2$ of the compressible flow simulation by solving the Poisson problem

$$U_1 = \frac{\partial \Psi}{\partial x_2}, \quad U_2 = -\frac{\partial \Psi}{\partial x_1}, \qquad \frac{\partial^2 \Psi}{\partial x_1^2} + \frac{\partial^2 \Psi}{\partial x_2^2} = -\omega .$$

One major source term of the system (7) is given by the term $\partial/\partial t(\rho_\infty \Phi)$, where $\rho_\infty \Phi$ matches in the limit of $M \to 0$ the incompressible pressure P, as shown in [2]. Neglecting the compressible viscous terms this quantity follows from the solution of

$$\frac{\partial^2 \Phi}{\partial x_1^2} + \frac{\partial^2 \Phi}{\partial x_2^2} = 2\left(\frac{\partial^2 \Psi}{\partial x_1^2}\frac{\partial^2 \Psi}{\partial x_2^2} - \left(\frac{\partial^2 \Psi}{\partial x_1 \partial x_2} \right)^2 \right), \tag{8}$$

which corresponds to the pressure poisson equation of an incompressible flow solver. From the source term filtering it follows that the pressure is identified as acoustic variable. In general, one would expect a decomposition of the pressure into an acoustic and a non-acoustic part called *pseudo sound pressure*. Note that the d'Alembert operator of the wave equation for the pressure as variable contains as a steady state limit the Laplacian operator and the related Lighthill equation changes in this limit into a Poisson equation for the pressure. Thus, it also contains the hydrodynamic near field. Due to the properties of $\rho_\infty \Phi$, however, this quantity is interpreted as pseudo sound pressure and the pressure is decomposed accordingly into

$$p = \rho_\infty \Phi + p^a ,$$

see also fig. 15. The primed perturbation density in (7) follows from the density decomposition

$$\rho = \rho_\infty + \rho' .$$

In general, it also describes non-acoustic quantities. The terms D_I, D_{II}, D_{III} on the left-hand side of the momentum equation are vorticity sinks, which cancel the vorticity generated due to acoustic/mean interaction on the left-hand side. In the limit $M \to 0$ the eqs. (7) match the formulation of Shen et al. (3) under the same assumption that entropy fluctuations can be neglected if low Mach number vortex sound is considered. The remaining differences are the vorticity sinks on the right-hand side of (7). Since the incompressible flow simulation does not contain the vorticity due to acoustic/mean interaction the missing sink terms allow the occurrence of this vorticity contribution as part of the acoustic computation. As these vorticity components occur in principle in the compressible base flow simulation, the additional sink terms are necessary to prevent the double computation of the discussed vorticity components.

The formulations used for the computations are obtained by introducing additional simplifications into the eqs. (7). The future goal is to use the method to predict turbulence related noise, where the unsteady base flow motion is mainly related to turbulent fluctuations. Neglecting the turbulent scattering of acoustic waves it seems to be acceptable to use a time averaged base flow field. Furthermore, for small acoustic fluctuations the non-linear terms can be dropped. Each vorticity sink term suppresses the vorticity generated by a related term on the left-hand side of (7). By simultaneously dropping the relevant left- and right-hand side terms, the generation of vorticity by the perturbation equations is prevented completely paying the price of neglecting

the acoustic source contribution of the left-hand side terms, too, which can be assumed to have a small influence. From this procedure the equations used for the computations read

$$\frac{\partial \rho'}{\partial t} + \frac{\partial}{\partial x_k}\left(\rho' \overline{U}_k + \rho_\infty u_k^a\right) = 0$$

$$\frac{\partial u_i^a}{\partial t} + \frac{\partial}{\partial x_i}\left(\overline{U}_k u_k^a\right) + \frac{1}{\rho_\infty}\frac{\partial p^a}{\partial x_i} = 0 \qquad (9)$$

$$\frac{\partial p^a}{\partial t} - c_\infty^2 \frac{\partial \rho'}{\partial t} = -\frac{\partial}{\partial t}\left(\rho_\infty \Phi\right).$$

4 Results and Discussion

The flow around a circular cylinder at Mach number *M=0.3* and Reynolds number *Re=200* was used as test problem to compare different formulations of perturbation equations. The direct simulation of the compressible flow was carried out using an AUSM scheme for spatial discretization. The O-grid had a radial extension of *r/d=80* cylinder diameters and a resolution of *657 x 513* grid points in the radial and circumferential direction, respectively. Fig. 2 shows the perturbation pressure obtained from the CFD simulation by subtracting the time averaged pressure field.

The acoustic computations were performed on an O-grid with *257 x 161* grid points. The pressure derivative was computed from the CFD solution using second-order central differences. One time period of the vortex shedding, non-dimensionalized with the cylinder diameter *d* and the far field sonic speed was *T=17.0.* The time period was split into 43 source time levels and during the acoustic simulation the time dependent source was computed by linearly interpolating between two adjacent source data time levels. The details of the test cases considered are given in table 1.

	Definition
Case A	Source term $-\partial p/\partial t$ from CFD, perturbation equations (4), kinematic solid wall BC
Case B	$-\langle \partial p/\partial t \rangle$, spatial filtering with $\sigma = 5.0$, perturbation equations (9), kinematic solid wall BC
Case C	$-\langle \partial p/\partial t \rangle$, spatial filtering with $\sigma = 20.0$, perturbation equations (9), kinematic s. wall BC
Case D	Source $-\partial(\rho_\infty \Phi)/\partial t$ (eqn. (8)), perturbation equations (9), kinematic solid wall BC
Case E	Source term (6), perturbation equations (5), H_i and H_p dropped, no-slip solid wall BC
Case F	Source term (6), perturbation equations (5), no-slip solid wall BC

Table 1: Descriptions of computational cases

Fig. 3 shows the computed perturbation pressure field at time level *T=200* using eqs. (4) and the pressure derivative from the compressible flow simulation (case A, table 1). Compared with fig. 2 it is obvious that the acoustic pressure levels are overpredicted by a factor of about three. Furthermore, the structure of the vortex street is visible in fig. 3 indicating that vorticity is generated through the acoustic simulation. Fig. 7 shows the vorticity for this case. Compared with the magnitudes of the CFD solution, fig. 6, the vorticity magnitude is unphysically high. Fig. 9 presents the pressure signal for case A in a receiving point *r/d=40* above the cylinder, indicating that the solution becomes unstable for *T>200.* The only source of vorticity is due to acoustic/mean interaction and this magnitude was presumed to be clearly smaller than the magnitude of the overall vorticity from the CFD solution. Obviously in conjunction with the gradients of the base flow instabilities are excited.

To prevent the occurrence of vorticity in the simulation at all the APE formulation has been used for the cases B, C, and D. For the cases B and C the source has been approximated by spatially filtering the time derivative of the pressure to circumvent the excitation of spurious acoustic signals due to the acoustic signals

contained in the compressible flow simulation. A Gaussian filter kernel was used to separate the important near field hydrodynamic sources from the far-field acoustic signals, i.e.

$$\frac{\partial}{\partial t}(\rho_\infty \Phi) \approx \left\langle \frac{\partial p}{\partial t} \right\rangle = \frac{\partial p}{\partial t} \exp\left(-\frac{(r-r_0)^2}{\sigma^2} \right). \tag{10}$$

Fig. 8 shows the magnitude of the vorticity obtained for case B. It is clearly visible that no vorticity occurs in the acoustic simulation but a small amount due to the boundary condition is visible in the vicinity of the cylinder. No vortex structures in the wake of the cylinder appear for cases B and C, figs. 4 and 5, respectively. Case C was computed using a large filter width of $\sigma = 20.0$ in (10). Fig. 5 shows that the acoustic pressure is still about three times too large. For a small filter width $\sigma = 5.0$ the magnitude of the acoustic pressure and the lobes tilted in the flow direction agree fairly well with the CFD solution. Nevertheless, in the CFD solution in fig. 2 a modulation of the pressure waves is evident in the upper and lower area downstream the cylinder. As indicated by the direct simulation of Hatakeyama [6] for the cylinder problem using a high order compact finite difference scheme, according to the cases B and C no secondary lobes do occur. Thus, it is fair to assume that the low order scheme used for the direct simulation might fail to resolve the acoustic field properly. Fig. 10 depicts the perturbation pressure of the CFD simulation along the intersection line *X=0* for different time levels *T* during one period of vortex shedding. A modulation of the pressure distribution is visible such that no common envelope can be identified in the figure. Furthermore, the decay of the pressure is smaller than $\propto r^{-1/2}$, pointing out the difficulties to resolve the acoustic field with common CFD tools.

Fig. 11 shows results of the various formulations described in table 1 for the decay of the pressure amplitudes. The curve related to case E is computed using the system (5) without the terms H_i and H_p. It is clear from fig. 11 that the acoustic pressure levels are underpredicted. Using the term H_i and H_p, case F, a large increase of the vorticity magnitudes in the computational solution is observed and the acoustic pressure levels are overpredicted. The result of case B and case D are computed applying the APE formulation. Case D is computed with the source according to eqn. (8), therefore the generation of spurious acoustic/acoustic signals is completely prevented. Case B is computed using a small filter width. The magnitudes of the pressure amplitudes are slightly smaller for case D, indicating that even with small spatial filter width used in case B still spurious acoustic signals are excited. The magnitudes of the pressure amplitudes of case B and D seem to be reasonable, compared with fig. 10. The directivity computed for the first harmonic frequency for case B is shown in fig. 12. Due to the mean flow the two lobes are tilted in the upstream direction. The result is compared with an analytical result for a 2D dipole in constant mean flow according to Guo [5]. The direction of the highest pressure amplitude follows to be $\theta \approx \pm 115^o$, which agrees fairly well with the computational result. Fig. 13 shows the decay of the effective pressure value for case B. In agreement with the asymptotic behavior of the 2D Green function, the pressure level decay is proportional to the power of *–1/2*.
Fig. 14 shows a contour plot of the pressure field for case D. Pressure levels as well as directivity agree quantitatively with the CFD solution in fig. 2.

5 Conclusion

Different formulations for a hybrid two step CFD/CAA approach have been investigated. As a 2D test case a laminar flow over a cylinder at Mach number 0.3 and Reynolds number 200 has been used. It was found that small vorticity sources due to acoustic/mean flow interaction in conjunction with a non-uniform mean flow are sufficient to generate excessive artificial vorticity in the acoustic solution. The generation of vorticity during the acoustic simulation can be successfully prevented when acoustic sources are used that solely excite acoustic modes in the governing equations. The evaluation of sources based on pressure derivatives from a compressible flow simulation yields large errors in the computed acoustic pressure levels due to the excitation of acoustic signals from acoustic signals contained in the CFD solution. The amplitude of the CAA computed acoustic signals could be reduced to a meaningful level if the acoustic source was spatially filtered in the vicinity of the cylinder to separate the essential hydrodynamic near field from the acoustic far field. An acoustic source has been computed using the vorticity of the compressible flow simulation. The occurrence of acoustic/acoustic generated spurious signals is suppressed completely. Applying this source the pressure magnitudes, the directivity of the computed sound field, and the decay of the pressure with increasing distance to the cylinder are reasonable.

6 Figures

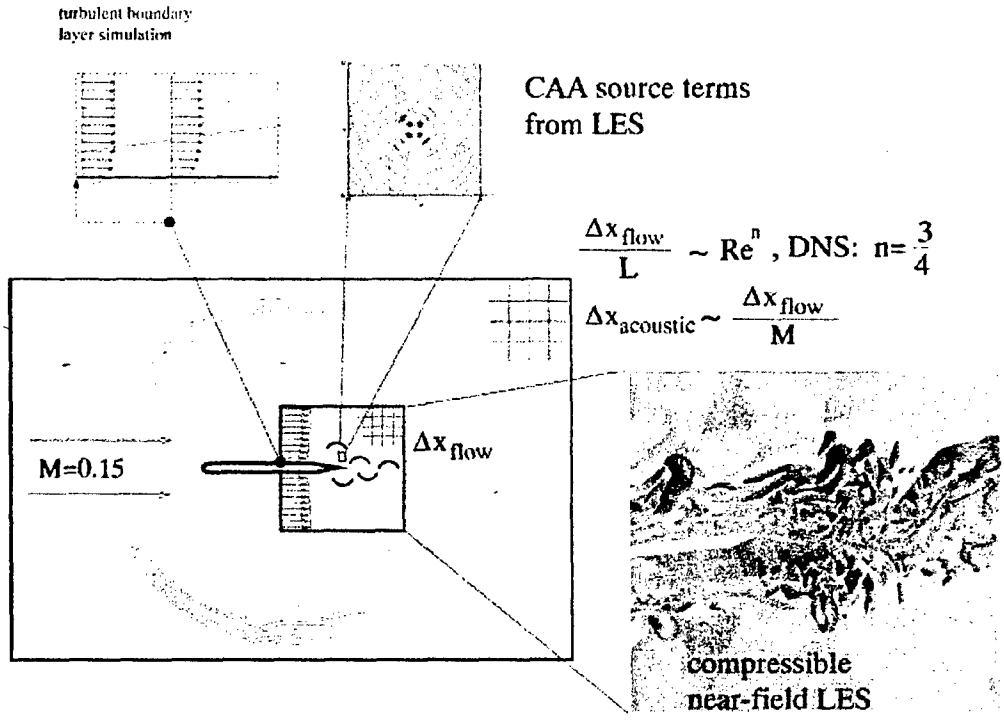

Fig. 1: Sketch of the computational domains to compute trailing edge noise with the hybrid approach; the CFD simulation resolves the vicinity of the trailing edge whereas the computational aeroacoustics (CAA) domain includes the whole airfoil section due to the less stringent demands concerning grid resolution thereby allowing to recognize scattering at the leading edge and the prediction of directivities

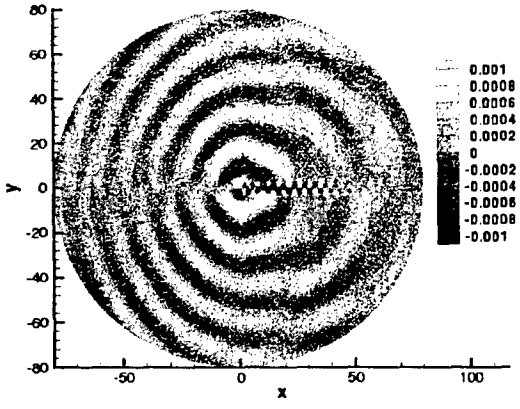

Fig 2: Perturbation pressure from the unsteady CFD simulation

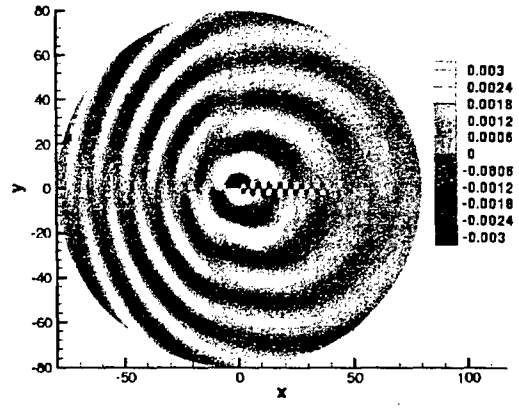

Fig. 3: Pressure from the CAA solution at time level T=200, Case A, tab. 1

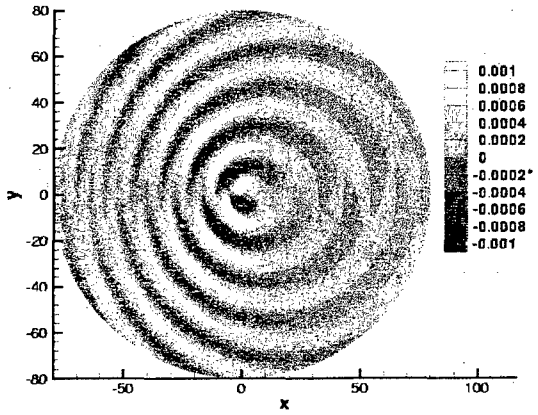

Fig. 4: Pressure from the CAA solution at time level *T=200,* Case B, tab. 1

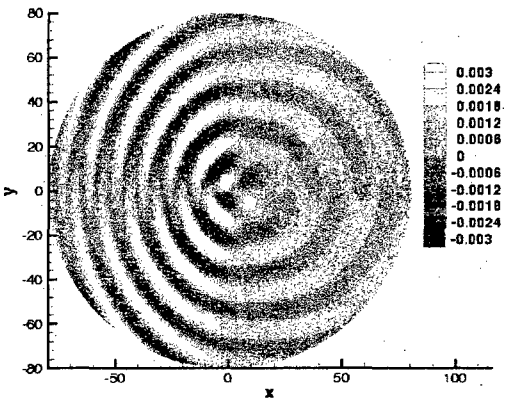

Fig. 5: Pressure from the CAA solution at time level *T=200,* Case C, tab. 1

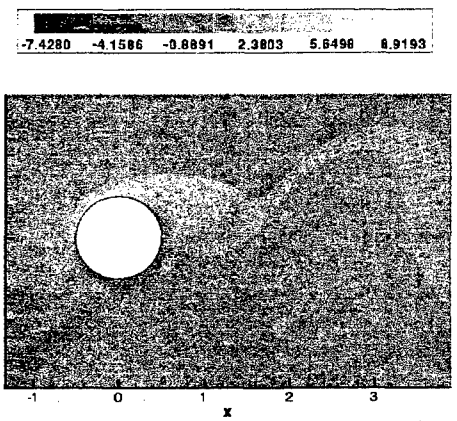

Fig. 6: Snapshot of the vorticity levels of the CFD solution

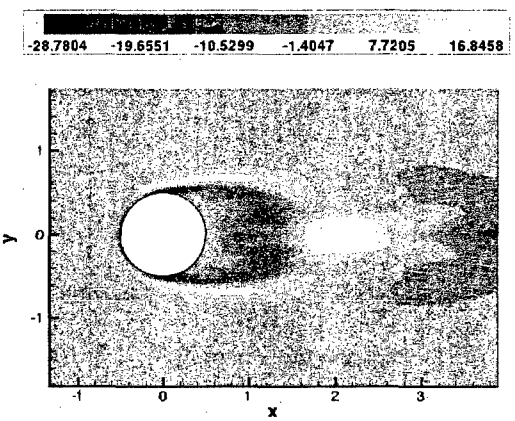

Fig. 7: Vorticity at time level T=200, CAA Solution Case A

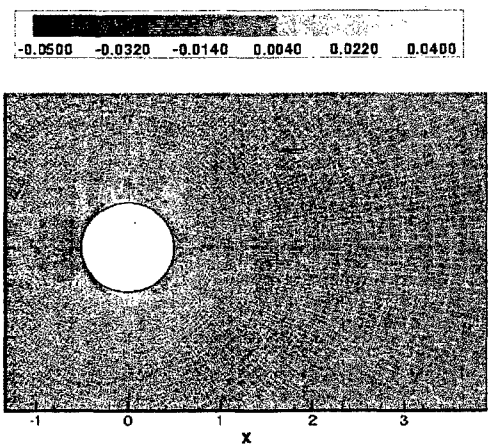

Fig. 8: Vorticity at time level T=200, CAA solution Case B

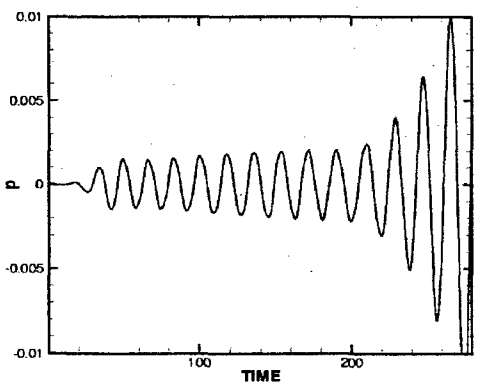

Fig. 9: Unstable pressure signal for a point at r/d=40 above the cylinder, Case A

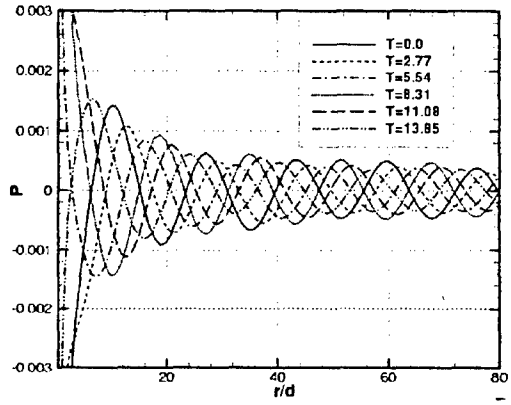

Fig. 10: Perturbation pressure from the unsteady CFD solution along line X=0

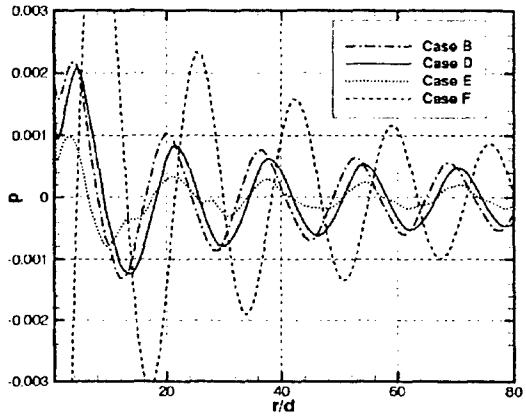

Fig. 11: Perturbation pressure on the intersection line X=0, CAA solutions

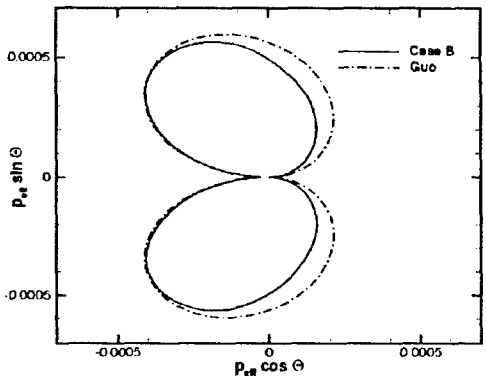

Fig. 12: Directivity for the first harmonic frequency

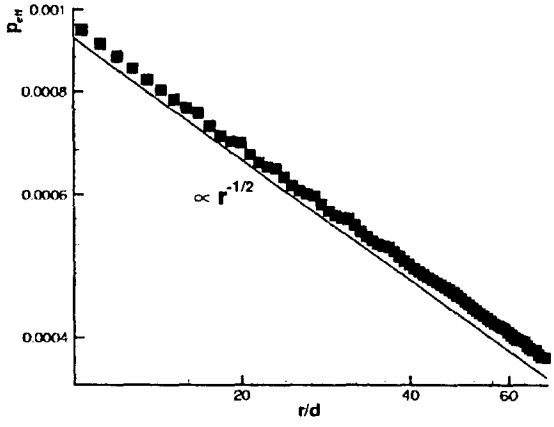

Fig. 13: Decay of the sound pressure perpendicular to the mean flow direction, Case B

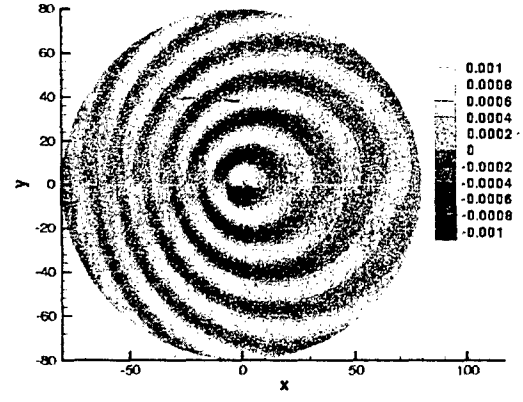

Fig. 14: Pressure from the CAA solution, source term $-\rho_\infty \partial\Phi/\partial t$, eqn. (8) (Case D)

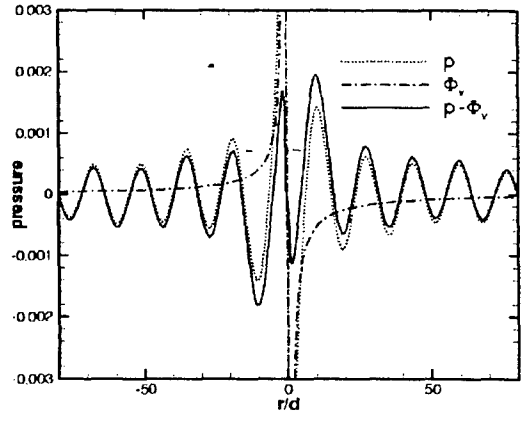

Fig. 15: Decomposition of the pressure with the pseudo sound pressure $\rho_\infty \Phi$ for a line X=0

Acknowledgments

This work was supported by the Bundesministerium für Bildung, Wissenschaft, Forschung und Technologie (BMBF) under grant number 20A9702B.

References

[1] C. Bailly, C. Bogey, and D. Juve. Computation of the flow noise using source terms in linearized Euler´s equations. 2000. AIAA Paper 2000-2047.

[2] R. Ewert, M. Meinke, W. Schröder. Comparison of Source Term Formulations for a Hybrid CFD/CAA Method. AIAA Paper 2001-2200, 2001.

[3] R. Ewert, W. El-Askary, M. Meinke, W. Schröder. Computation of turbulence related noise on the basis of large-eddy simulation. In H. Koerner, W. Delfs, editors, *Second Aeroacoustic Workshop*, 2001.

[4] R. Ewert, M. Meinke, W. Schröder. Aeroacoustic source terms for the linearized Euler equations. AIAA Paper 2000-2046, 2000.

[5] Y. P. Guo. Application of the Ffowcs Williams/Hawkings equation to two dimensional problems. J.Fluid Mech. 403, pp 201-221, 2000.

[6] N. Hatakeyama, H. Hosoy, O. Inoue. DNS of Sound generated by Cylinder Wakes. Computational Fluid Dynamics 2000. N. Satofuka (Ed.). Springer 2001.

[7] H. S. Ribner. Perspectives on jet noise. AIAA Paper 81-0428. 1981.

[8] W. Schröder, M. Meinke, R. Ewert, W.A. El-Askary. LES of a turbulent flow around a sharp trailing edge. Proc. Workshop on Direct and Large Eddy Simulation IV, July 18-21, 2001, Kluwer Academic Publishers.

[9] S. Sarkar, M.Y. Hussaini. Computation of the acoustic radiation from bounded homogeneous flows. In J.C. Hardin, M.Y. Hussaini, editors, *Computational Aeroacoustics*, pages 335-349. Springer, 1993.

[10] C. Tam, J. Webb. Dispersion-relation-preserving finite difference schemes for computational acoustics. J. Comput. Phys., 107, pp. 262-281, 1993.

[11] F. Q. Hu, M.Y. Hussaini, J.L. Manthey. Low-dissipation and low-dispersion Runge-Kutta schemes for computational acoustics. J. Comput. Phys. 124, pp 177-191, 1996.

[12] C. Tam , Z. Dong. Wall boundary condition for high-order finite-difference schemes in computational aeroacoustics. Theoretical and Computational Fluid Dynamics Vol. 6, No. 6, pp 303-322, 1994.

[13] C. Tam , Z. Dong. A study of the short wave components in computational acoustics. Journal of Comput. Acoustics, Vol. 1, No. 1, pp 1-30, 1993.

[14] J.C. Hardin, D.S. Pope. Sound generation by flow over a two-dimensiona l cavity. AIAA Journal 33/6, pp 407-412, 1995.

[15] J.C. Hardin, D.S. Pope. An acoustic/viscous splitting technique for computational aeroacoustics. Theoret. Comput. Fluid Dynamics 6, pp. 323-340, 1994.

[16] W.Z. Shen, J.N. Sorensen. Aeroacoustic modelling of low-speed flows. Theoret. Comput. Fluid Dynamics 13, pp. 271-289, 1999.

[17] W.Z. Shen, J.N. Sorensen. Comment on the aeroacoustic formulation of Hardin and Pope. AIAA Journal 37, pp. 141-143, 1999.